



HAL
open science

Modelling potential/current distribution in microbial electrochemical systems shows how the optimal bioanode architecture depends on electrolyte conductivity

Rémy Lacroix, Serge Da Silva, Monica Viaplana Gaig, Raphaël Rousseau, Marie-Line Délia-Dupuy, Alain Bergel

► To cite this version:

Rémy Lacroix, Serge Da Silva, Monica Viaplana Gaig, Raphaël Rousseau, Marie-Line Délia-Dupuy, et al.. Modelling potential/current distribution in microbial electrochemical systems shows how the optimal bioanode architecture depends on electrolyte conductivity. *Physical Chemistry Chemical Physics*, 2014, 16 (41), pp.22892-22902. 10.1039/C4CP02177K . hal-01919588

HAL Id: hal-01919588

<https://hal.science/hal-01919588>

Submitted on 12 Nov 2018

HAL is a multi-disciplinary open access archive for the deposit and dissemination of scientific research documents, whether they are published or not. The documents may come from teaching and research institutions in France or abroad, or from public or private research centers.

L'archive ouverte pluridisciplinaire **HAL**, est destinée au dépôt et à la diffusion de documents scientifiques de niveau recherche, publiés ou non, émanant des établissements d'enseignement et de recherche français ou étrangers, des laboratoires publics ou privés.



Open Archive Toulouse Archive Ouverte (OATAO)

OATAO is an open access repository that collects the work of Toulouse researchers and makes it freely available over the web where possible

This is an author's version published in: <http://oatao.univ-toulouse.fr/20238>

Official URL: <https://doi.org/10.1039/C4CP02177K>

To cite this version:

Lacroix, Rémy and Silva, Serge Da and Viaplana Gaig, Monica^{ORCID} and Rousseau, Raphaël^{ORCID} and Délia, Marie-Line^{ORCID} and Bergel, Alain^{ORCID}
Modelling potential/current distribution in microbial electrochemical systems shows how the optimal bioanode architecture depends on electrolyte conductivity. (2014) *Physical Chemistry Chemical Physics*, 16 (41). 22892-22902. ISSN 1463-9076

Any correspondence concerning this service should be sent to the repository administrator: tech-oatao@listes-diff.inp-toulouse.fr

Modelling potential/current distribution in microbial electrochemical systems shows how the optimal bioanode architecture depends on electrolyte conductivity

Rémy Lacroix,^{*a} Serge Da Silva,^a Monica Viaplana Gaig,^b Raphael Rousseau,^b Marie-Line Délia^b and Alain Bergel^b

The theoretical bases for modelling the distribution of the electrostatic potential in microbial electrochemical systems are described. The secondary potential distribution (*i.e.* without mass transport limitation of the substrate) is shown to be sufficient to validly address microbial electrolysis cells (MECs). MECs are modelled with two different ionic conductivities of the solution (1 and 5.3 S m⁻¹) and two bioanode kinetics ($j_{\max} = 5.8$ or 34 A m⁻²). A conventional reactor configuration, with the anode and the cathode face to face, is compared with a configuration where the bioanode perpendicular to the cathode implements the electrochemical reaction on its two sides. The low solution conductivity is shown to have a crucial impact, which cancels out the advantages obtained by setting the bioanode perpendicular to the cathode. For the same reason, when the surface area of the anode is increased by multiplying the number of plates, care must be taken not to create too dense anode architecture. Actually, the advantages of increasing the surface area by multiplying the number of plates can be lost through worsening of the electrochemical conditions in the multi-layered anode, because of the increase of the electrostatic potential of the solution inside the anode structure. The model gives the first theoretical bases for scaling up MECs in a rather simple but rigorous way.

DOI: 10.1039/c4cp02177k

1. Introduction

A huge amount of chemical energy is available in the large variety of organic matter contained in sediments, effluents, agricultural residues and various other types of biomass that are commonly unexploited or even have to be treated at the cost of high energy expenditure.¹ Nevertheless, tools are lacking to tap into these free resources and transform the chemical energy they contain into electricity or fuels. Microbial electrochemical systems (MESs) may offer amazing innovative ways to move towards the exploitation of such resources. MESs are based on the recently discovered capability of some microorganisms to catalyse the electrochemical oxidation of organic matter. Among MESs, microbial fuel cells that transform chemical energy directly to electricity have been the most widely investigated since 2002, but they still seem quite far from large size applications. Microbial electrolysis cells (MECs) use the same

technology to produce hydrogen by associating a microbially-catalysed bioanode with an abiotic cathode for hydrogen evolution.^{2,3} MECs can thus produce hydrogen from the oxidation of organic matter. They probably constitute the most technologically advanced application of MESs at present.

Scientific research on MESs has advanced at an impressive pace in the laboratory⁴ and a major challenge is now to bring these technologies into application and engineer practical systems at larger scales. The experimental studies that have dealt with MES scale-up have shown the great difficulty of this challenge,⁵⁻⁹ for which there is no map or compass but the experimental approach. They have generally observed a considerable, unavoidable decrease in performance when the size of the devices increases.

In many respects, theoretical approaches have succeeded in deciphering the mechanisms of electron transfer pathways inside electroactive biofilms. For instance, numerical modelling has shown that transfer *via* diffusible extracellular mediators can generate only small current densities because of the rate-limiting diffusion step. Theoretical diffusion-limited current densities of 0.13¹⁰ or 0.21 A m⁻² (ref. 11) have been calculated, which are more than an order of magnitude lower than values commonly recorded experimentally, and consequently point to the occurrence of other

^a 6TMIC Ingénieries, 4 rue Brindejont des Moulinais, 31500 Toulouse, France.

E-mail: remy.lacroix@6t-mic.com; Fax: +33 (0)5 3443 6339;

Tel: +33 (0)5 3443 6339

^b Laboratoire de Génie Chimique, CNRS - Université de Toulouse (INPT),

4 allée Emile Monso, BP84234, 31432 Toulouse, France.

E-mail: alain.bergel@ensiacet.fr; Tel: +33 (0)5 3432 3673

electron transport pathways. Models have been designed assuming that the extracellular biofilm matrix has conductive properties that obey Ohm's law.^{12,13} Electron transport through electron hopping along chains of immobilized redox compounds (type *c* cytochromes for example) has also been put forward, and a unified modelling approach has been described that groups together all electron transport mechanisms under an apparent electron diffusion coefficient.^{14,15} Numerical modelling has supported considerable advances in understanding the behaviour of microbial anodes in many other respects, such as the crucial role of proton transfer from the biofilm¹⁶ or differentiating charge accumulation and electron transfer.¹⁷

New laws of electro-microbial kinetics have been introduced by combining the electrochemical Nernst¹² or Butler–Volmer¹⁸ law with the Monod law. The conventional electrochemical kinetics was thus modified to take account of the specific relationship between substrate concentration and metabolic rate. From a formal point of view, it would be more correct to refer to the Michaelis–Menten law to express the relationship between substrate concentration and respiration rate, rather than to the Monod law, which is related to cell growth. Nevertheless, whatever the name, the mathematical expression remains the same. The Nernst–Monod expression has then been implemented to model low scan rate cyclic voltammetry.^{19–21}

These various models have supported brilliant results in deciphering interfacial electro-microbial mechanisms but their contribution to advances in scaling up reactor architectures remains limited because their application domain is restricted to the biofilm zone. The reactor architecture, located beyond the biofilm/solution interface, is not taken into account.

Numerical models that address the interfacial phenomena tacitly assume that the Nernst potential (E) is uniform on the electrode surface. In other words, it is assumed that the current has a uniform value over the entire electrode surface. Actually, this hypothesis is strictly valid only in analytical cells that are designed specifically with this objective, such as two flat electrodes set face to face with surface areas equal to the cross-section of the cell. Uniformity of current distribution is far from being valid in most of the electrochemical cells commonly used in the laboratory. The situation is exacerbated in industrial reactors, which generally aim at creating locally non-uniform current distributions to increase their performance. The morphology of industrial electrodes (perforated plates, expanded metal, grids. . .) is so designed to favour the high local currents that are promoted by electrode edges.

On the one hand, it is very important to be aware that non-uniform current distributions may occur in lab cells, so as to be able to discuss the bias they may introduce in the conclusions. On the other hand, modelling current distribution is an essential prerequisite in the design of industrial prototypes and units. The purpose of the work presented here was to give an initial basis for modelling current distribution in microbial electrochemical systems, taking a microbial electrolysis cell (MEC) for hydrogen production as an example. The distributions of potential and current were modelled in the electrolyte, using the kinetics of the microbial anode as a boundary condition.

The metabolic rates, the kinetics of electron transport or mass transfer inside the biofilm or in the porosity of the electrode structure, if a porous anode is implemented, were not modelled directly but were included in the kinetic law relating to the microbial anode. The purpose of the work was to demonstrate to what great extent the electrode configuration can impact the performance of a MEC depending on the ionic conductivity of the medium.

2. Theoretical aspects

2.1 Electrostatic and Nernst potentials

The variation of the electrostatic potential (ϕ) in a phase that does not include any source or sink of charges is governed by the Laplace equation:

$$\Delta\phi = 0 \quad (1)$$

This equation, solved in the whole space of an electrochemical reactor, leads to the field of electrostatic potential, from which the local currents can be extracted at any point through Ohm's law applied to electrolytes:

$$i = -\sigma \text{grad } \phi \quad (2)$$

The model first solves eqn (1) in the whole reactor space to obtain the potential distribution and then calculates the current distribution by eqn (2). The total current that flows through the reactor is finally calculated by integrating the local current over the anode or the cathode surface.

The integration space may include different electrolytes, including separators or membranes, which are taken into account as adjacent spaces, each with its own value of conductivity. The integration space is bounded by two types of limits: the electrodes and the insulating reactor walls. At the reactor walls the flux is zero, *i.e.* the derivative normal to the wall is equal to zero (Neumann boundary condition):

$$\text{grad } \phi \cdot \vec{n} = 0 \quad (3)$$

It should be emphasized that the Laplace equation is valid only inside spaces in which no charge is produced or consumed by reactions. Solving the Laplace equation is consequently the usual way to describe potential distribution in the electrolytes of electrochemical reactors. In the case of MESs, the Laplace equation cannot be applied inside the biofilm, in which several ionic species are produced or consumed. The Poisson equation must be used:

$$\Delta\phi = -\sigma \text{div}(i) \quad (4)$$

and its numerical solution is considerably more complex. Determining the potential distribution in a MES by including the biofilm(s) in the integration space needs the Poisson equation to be solved. It would be a cumbersome approach to MES modelling, while the Poisson equation is only required in the very small spaces represented by the biofilm(s). In the present work, we excluded the biofilm from the integration space and included all the steps related to the biofilm kinetics in the electrochemical boundary condition (Fig. 1). It was thus possible to get the potential distribution by solving the Laplace

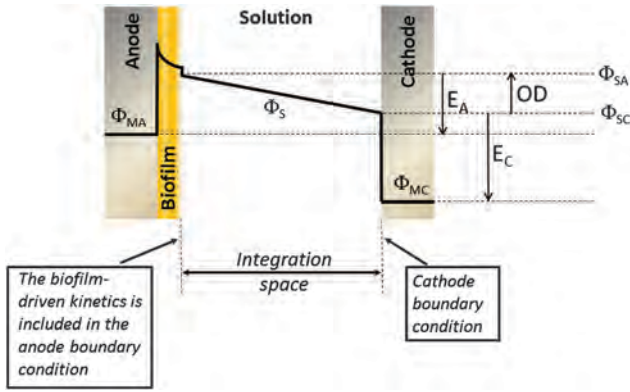


Fig. 1 Scheme of the distribution of the electrostatic potential (ϕ) in an MEC. At the cathode–solution interface, the Nernst potential is given by the difference in electrostatic potential between the electrode material and the solution ($E_C = \phi_{MC} - \phi_{SC}$). For the bioanode, the Nernst potential includes the potential gradient inside the biofilm by locating the interface at the biofilm–solution frontier ($E_A = \phi_{MA} - \phi_{SA}$). The ohmic drop (OD) was assumed to be linear in the bulk in the absence of separator.

equation. Another advantage of this approach was to take benefit of the theoretical and experimental studies that have developed kinetics for microbial bioanodes,^{12,18} which can so be used as the boundary conditions.

It was assumed in the present work that anode and cathode materials were efficient electrical conductors or, similarly, that current collectors were efficient enough for the potential drop inside the electrode materials be neglected. This assumption is valid for most electrodes used in MESSs. It may no longer be applicable in some cases, when the electrodes show significant electrical resistance, for example, or with flow-through 3-dimensional electrodes. In such particular cases, the potential drop inside the electrode material itself should be taken into account. Here, the potentials of the anode (ϕ_{MA}) and cathode (ϕ_{MC}) materials were uniform and their difference was equal to the voltage applied to the MEC (U_{cell}):

$$U_{cell} = \phi_{MA} - \phi_{MC} \quad (5)$$

At the electrode surface, the difference between the potential of the electrode material (ϕ_M) and the potential of the electrolyte in contact with the electrode surface (ϕ_S) is defined as the Nernst potential (E):

$$E_A = \phi_{MA} - \phi_{SA} \quad (6)$$

$$E_C = \phi_{MC} - \phi_{SC} \quad (7)$$

Actually, in the field of electroactive biofilms, the Nernst potential is tacitly taken as the difference of the electrostatic potential in the electrode material and the electrostatic potential at the biofilm/solution interface, instead of the rigorous drop of electrostatic potential at the electrode surface (Fig. 1). Only very rare theoretical studies have dealt with the electrostatic potential drop inside electroactive biofilms.¹³ Furthermore, all experimental potential values are expressed and measured according to the tacit assimilation of the electrode surface with the biofilm/solution interface. This approach was also used in the present model for the microbial anode.

2.2 Primary, secondary and tertiary potential distributions

The boundary conditions at the biofilm/solution interface can be established in three different ways, which define the primary, secondary and tertiary potential and current distributions.

Primary potential distribution. The simplest approach assumes that a thermodynamic equilibrium is achieved at the electrodes:

$$E_A = E^{0'} \text{ of the anodic redox system} \quad (8)$$

$$E_C = E^{0'} \text{ of the cathodic redox system} \quad (9)$$

Dirichlet boundary conditions are thus obtained, which allow an analytical solution to be found for a few simple cell geometries. The primary distribution obtained describes the potential distribution at equilibrium, *i.e.* when no current flows through the cell. Under such conditions, because the current is nil, the conductivity of the electrolyte(s) has no influence. The potential distribution depends only on the geometry of the cell. The primary distribution is a useful simple approach but it gives only elementary information on the potential distribution far from real operation conditions.

Secondary potential and current distributions. The secondary distribution is obtained by using the electrochemical kinetics law related to each electrode:

$$j = f_A(E_A) \quad (10)$$

$$j = f_C(E_C) \quad (11)$$

Using Ohm's law (eqn (2)) and taking into account the fact that j is a vector normal to the electrode surface gives the boundary conditions:

$$-\sigma \text{ grad } \phi|_{SA} = f_A(E_A)\vec{n} \quad (12)$$

$$-\sigma \text{ grad } \phi|_{SC} = f_C(E_C)\vec{n} \quad (13)$$

The kinetics laws can be a conventional Butler–Volmer or Tafel equation, a specific equation established for microbial bioanodes^{12,18} or any phenomenological j – E correlation determined under appropriate operating conditions.

The secondary distribution takes the activation overpotential due to electron transfer kinetics into account. In the case of a microbial anode, the specific biofilm or metabolic overpotentials²² related to biofilm electrocatalysis are also included in the electrode boundary conditions (eqn (10)). Similarly, the possible effect of protons mass transfer on the mechanism of biofilm electrocatalysis¹⁶ is also considered to be part of the bioelectrode kinetics and is included in the boundary conditions. The secondary distribution does not consider the effect of external mass transfers that may occur in solution. In the case of a microbial electrode, it is thus assumed that the concentrations at the biofilm/solution interface are equal to the concentrations in the bulk of the solution. Care must consequently be taken to use boundary conditions that are valid for the bulk concentrations used in the model. The secondary distributions are suitable when mass transfers in solution are not rate-limiting, *e.g.* reactors that operate at low currents.

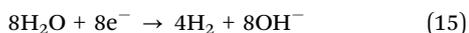
Tertiary potential and current distributions. The tertiary distribution includes mass transfer in solution. The boundary conditions at the electrodes take account of the value of the local concentrations at the electrode/solution or biofilm/solution interfaces. As the local concentrations depend on the local currents and the currents depend on the local concentrations, the potential and concentration fields must be solved concomitantly. This is obviously the most accurate approach but it considerably increases the computational complexity. It is consequently implemented only when necessary, particularly when current densities are so high that mass transport in the solution does not manage to compensate for the substrate consumption.

3. Results and discussion

The present work deals with a common microbial electrolysis cell (MEC) composed of a microbial anode that achieves acetate oxidation:



associated with a stainless steel abiotic cathode that produces hydrogen by water reduction:



The general theory of such an MEC has already been detailed^{2,3} and numerous experimental approaches have been reported that have used this system. Here, a stainless steel cathode was used because of the particular catalytic property of this material for hydrogen evolution when associated with weak acids.^{23,24} For the sake of simplicity, a single compartment device was considered. Nevertheless, a separator could easily be introduced into the model as a thin supplementary space characterized by its specific conductivity.

3.1 Assessment of the impact of external mass transfer on microbial bioanodes

The first phase of model design consisted of choosing between the secondary and tertiary approaches. To do this, the possible impact of external mass transfer must be assessed. At the stationary state, the molar flux of acetate (Φ_{acetate}) at the biofilm/solution interface is correlated to the current density by:

$$\Phi_{\text{acetate}} = j/8F \quad (16)$$

where F is the Faraday constant. In solution, the acetate flux is expressed by:

$$\Phi_{\text{acetate}} = D_{\text{acetate}}(C_{\text{acetate}}^{\text{B}} - C_{\text{acetate}}^{\text{int}})/\delta \quad (17)$$

where δ is the thickness of the diffusion layer. In a quiescent solution, the thickness of the diffusion layer, which is controlled by natural convection, can be assumed to be 100–200 μm on flat electrodes.^{25–27} Thicknesses are smaller in stirred solutions. It seems to be agreed that the maximum current density that can be reached with flat microbial bioanodes is of the order of 10 to 15 A m^{-2} .^{28,29} Higher current densities have been reached with

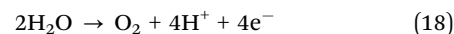
specific surface morphologies,^{20,29,30} ultra-microelectrodes,³¹ or 3-dimensional multi-layered electrodes,³² but flat plated bioanodes give a maximum close to 15 A m^{-2} .

Taking a high value of current density ($j = 15 \text{ A m}^{-2}$) associated with slow mass transfer in the solution, *i.e.* a large diffusion layer thickness ($\delta = 200 \mu\text{m}$) eqn (16) and (17) lead to a maximum concentration gradient ($C_{\text{acetate}}^{\text{B}} - C_{\text{acetate}}^{\text{int}}$) of 3.1 mM. It has been reported for different microbial bioanodes that the current density varies with acetate concentration according to a Michaelis–Menten type law, with a half-maximum-rate concentration around 3 mM¹⁹ or with maximum currents reached at concentrations above approximately 5 mM.¹⁸ If the acetate concentration in the bulk is high enough, equal to or above 10 mM for instance, the bioanode kinetics is not altered by the concentration gradient at the biofilm/solution interface. This evaluation shows that mass transfer in solution does not significantly affect the kinetics of microbial bioanodes provided that the acetate concentration is kept high enough in the bulk.

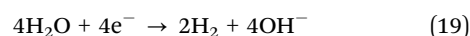
On the other hand, the abiotic cathode ensures that water reduction is not rate-limited by mass transfer of the reactant. The secondary distribution is therefore appropriate to model an MEC that operates at sufficiently high substrate concentration. The present work consequently developed a secondary distribution approach. From a general point of view, a secondary distribution model needs only a few input parameters: the description of the reactor geometry associated with the conductivity of each zone when a membrane or several compartments are involved, and the equations that constitute the boundary conditions for the two electrodes (eqn (10) and (11)). Then, solving eqn (1) and (2) leads to the potential and current distribution in the whole reactor space.

3.2 Validation of the numerical process with abiotic electrolysis of water

The numerical process was validated using a simple experimental system that performed conventional water electrolysis, *i.e.* the oxidation of water to oxygen at the anode:



and the reduction of water to hydrogen at the cathode:



The electrolyte contained Na_2SO_4 , the concentration of which was varied to obtain conductivities of 0.85, 2.41 and 4.25 S m^{-1} . For each conductivity, the stationary cell voltages were measured during electrolysis performed under potentiostatic conditions with current densities varying from 0 to 250 A m^{-2} and (Fig. 2).

The current–potential correlations (j – E), which were required as input for the secondary-type model, were determined experimentally for the anode and the cathode. The anodic and cathodic experimental (j – E) curves were fitted by polynomial equations that were used as boundary conditions (eqn (12) and (13)). The model was then run with the three values of conductivity to calculate the theoretical variation of the current density with the cell voltage, plotted in Fig. 2.

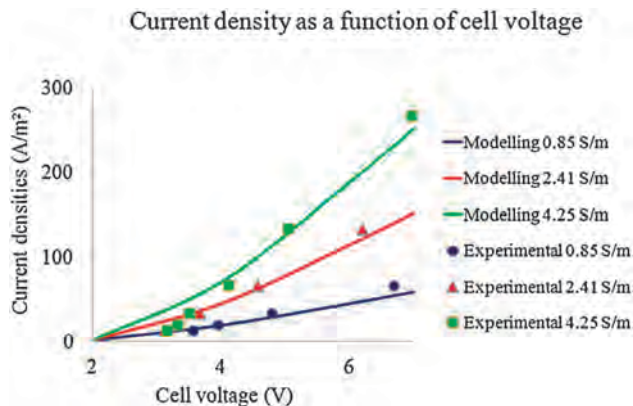


Fig. 2 Comparison of theoretical (curves) and experimental (symbols) results for water electrolysis. Conventional water electrolysis was performed using a stainless steel parallel anode and a cathode in potentiostatic mode for various values of the current. The ionic conductivity of the solution was adjusted through the concentration of sodium sulphate.

It should be noted that the theoretical results were obtained without numerical adjustment of any physical parameter value. The experimental anode and cathode kinetics (j - E curves) were used to feed the model. Then the model gave directly the theoretical current-voltage data according to the geometry of the cell and the value of conductivity. The theoretical curves were in very good agreement with the experimental data, showing the perfect validity of the model over a large range of cell voltages and current densities.

3.3 Modelling MEC with parallel or perpendicular electrodes

Model feeding: reactor geometry, solution conductivity and boundary conditions. The model considered a single-chamber MEC, in which acetate oxidation (reaction (14)) was achieved by a microbial anode and hydrogen evolved at an abiotic cathode (reaction (15)). Most electrolytes used in MEC, and more largely in MES, contain buffers, usually potassium or sodium phosphates, and salts required for microbial growth (ammonium, acetate, *etc.*).^{3,33-36} Common values of conductivity of these electrolytes are of the order of 1 S m^{-1} . A particular branch of MES studies deals with marine systems. In this framework, a conductivity of 5.3 S m^{-1} corresponding to seawater at 25°C can be used.³⁷ These two values of conductivity were chosen as standards for further studies.

The cathode boundary condition was determined experimentally using a stainless steel cathode in a solution containing 10 mM phosphate buffer. It has been reported that MEC cathodes benefit from the presence of phosphate species or other weak acids.^{23,24} These species act as homogeneous catalysts of water reduction in a mechanism called electrochemical deprotonation.³⁸ The experimental j - E curve was transformed into a polynomial function that was introduced into the model. In order to be consistent with the maximum value chosen for conductivity, the bioanode kinetics corresponded to a microbial anode formed in seawater from marine sediment. The anode current-potential curve available in the literature³⁹ gave a maximum current density of 5.8 A m^{-2} at $+0.1 \text{ V/SCE}$.

The experimental j - E curve was fitted with a polynomial function to be used numerically. This anode kinetics corresponded to current density values commonly obtained in the state of the art of the domain and it could be implemented at the highest electrolyte conductivity contemplated here. It was consequently used as the “standard” anode kinetics for all calculations in the present work. Nevertheless, a more efficient kinetics was also used in some cases for comparison at low electrolyte conductivity. This anode followed a Nernstian electron transfer and allowed current densities around 34 A m^{-2} be reached from potentials as low as -0.3 V/SCE . It was extracted from the literature³⁰ and was fitted with a Nernst-Monod equation:

$$j = j_{\max} / \{1 + \exp(-F/RT(E_A - E_{1/2}))\} \quad (20)$$

where $j_{\max} = 34 \text{ A m}^{-2}$ is the maximum current density at the plateau and $E_{1/2} = -0.375 \text{ V/SCE}$ is the potential for which j is equal to half the j_{\max} value.

Two MEC geometries were considered: face to face parallel cathode and anode, and horizontal anode(s) perpendicular to a vertical cathode. Both anode and cathode were flat square plates with 10 cm sides whatever the configuration. The cathode was kept vertical in each configuration because this position is a suitable one for hydrogen evolution. It can logically be predicted that the whole performance should be limited by the microbial bioanode (reaction (14)) rather than the abiotic cathode (reaction (15)). It was consequently hoped that the perpendicular configuration would multiply the current produced by a factor of around 2 by allowing both sides of the anode to work (Fig. 3). Furthermore, this configuration allowed several anodes to be arranged facing the cathode if the anode kinetics was severely rate-limiting.

The results are discussed here in terms of current provided by the MEC. Identical conclusions would be drawn in terms of hydrogen production, assuming that the hydrogen flow rate is straightforwardly proportional to the current flowing through the reactor.

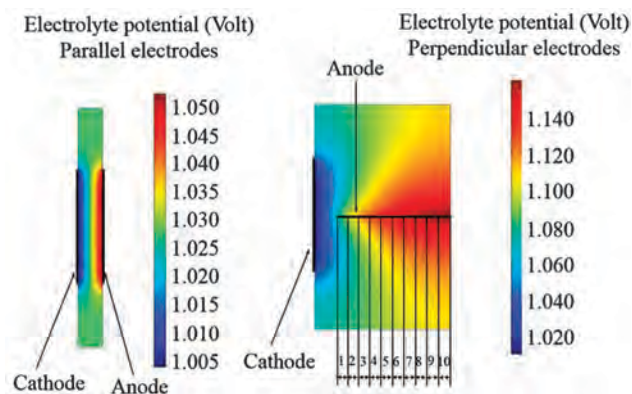


Fig. 3 Distribution of the electrostatic potential in solution (ϕ_s) in an MEC with parallel and perpendicular electrodes. The inter-electrode distance was 2 cm , cell voltage was 0.8 V , and conductivity was 1.0 S m^{-1} . The “standard” anode kinetics of a marine bioanode ($j_{\max} = 5.8 \text{ A m}^{-2}$) was used as the anode boundary condition. The red colour indicated a higher ϕ_s , *i.e.* a lower Nernst potential of the anode (E_A). For the perpendicular configuration, E_A increased fast with the distance from the cathode, showing that the anode working conditions deteriorated with the distance from the cathode.

Potential and current distributions. Fig. 3 compares the potential distribution in MECs with parallel or perpendicular electrodes at an identical inter-electrode distance of 2 cm, cell voltage of 0.8 V and conductivity of 1.0 S m^{-1} . The two MECs showed very different potential distributions. In the parallel configuration, the electrolyte potential was uniform along the electrode, with only small edge effects at the two extremities. The cathodic and anodic current densities were consequently uniform along the electrodes. In contrast, the perpendicular configuration showed a potential gradient along the anode indicating that the anode was not working at the same potential along its whole length.

The colour scale in Fig. 3 gives the values of the electrostatic potential in solution (ϕ_s). The Nernst potentials (E) can be extracted using eqn (5) to (7). The value of the electrostatic potential in the cathode material (ϕ_{MC}) was chosen as the basis of calculations and taken equal to zero, so that:

$$U_{\text{cell}} = \phi_{MA} \quad (21)$$

$$E_A = U_{\text{cell}} - \phi_{SA} \quad (22)$$

$$E_C = -\phi_{SC} \quad (23)$$

The electrostatic potential in the solution in close contact with the anode surface (ϕ_{SA}) varied from 1.070 to 1.159 V along the anode surface from the point nearest (2 cm) the cathode surface to the most distant point (12 cm). The anode Nernst potential (E_A) consequently decreased from -0.270 to -0.359 V with the distance from the cathode. The surface of the anode worked under less effective conditions due to the increasing ohmic drop as the distance from the cathode increased.

As indicated in Fig. 3, the anode was divided into ten parts of equal length (1 cm), numbered from 1 (nearest the cathode) to 10 (farthest from the cathode), and the current was integrated for each individual part. The current densities in each zone were compared for the two electrolyte conductivities of 1.0 and 5.3 S m^{-1} and two different anode boundary conditions: either the “standard” marine bioanode kinetics ($j_{\text{max}} = 5.8 \text{ A m}^{-2}$) or the more efficient Nernstian kinetics ($j_{\text{max}} = 34 \text{ A m}^{-2}$) (Fig. 4). In each case, the current density decreased along the anode length when the distance from the cathode increased. For less efficient “standard” bioanode kinetics and the high value of conductivity (5.3 S m^{-1}) the current density was almost uniform along the anode. In contrast, the low conductivity (1 S m^{-1}) induced a clear loss of performance along the anode surface: the first 10% of the anode closest to the cathode (zone 1) produced 14.3% of the total current, whereas the farthest 10% anode zone accounted for only 8.0%. This situation was even more dramatic with a more efficient bioanode, where the first zone produced 28.0% of the total current while the most distant produced only 5.2% (efficient kinetics with $j_{\text{max}} = 34 \text{ A m}^{-2}$ and conductivity 1 S m^{-1}). The potential gradient induced by the ohmic drop became a more severe problem as the performance of the bioanode increased. Furthermore, as shown in Fig. 4, increasing the conductivity of the electrolyte to 5.3 S m^{-1} with the

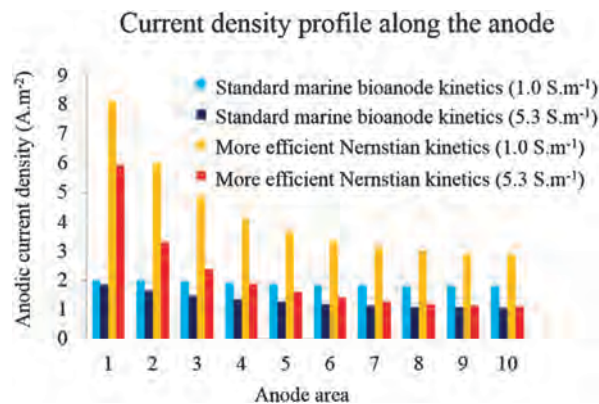


Fig. 4 Current density profiles along the anode in perpendicular configuration. The anode was divided into 10 zones from 1 (nearest to the cathode) to 10 (see Fig. 3). The current density in each zone was calculated (one side only) with two electrolyte conductivities, 1.0 and 5.3 S m^{-1} , and two different anode boundary conditions: either the “standard” marine bioanode kinetics ($j_{\text{max}} = 5.8 \text{ A m}^{-2}$) or the more efficient Nernstian kinetics ($j_{\text{max}} = 34 \text{ A m}^{-2}$). All calculations were performed with 2 cm inter-electrode distance and 0.8 V cell voltage.

efficient bioanode kinetics did not avoid the loss of performance along the anode length.

These calculations highlight the stumbling block represented by the low ionic conductivity of the electrolytes that are commonly used in MESs. Actually, many microorganisms do not accept high salt concentrations because of their sensitivity to osmotic pressure. Above a certain threshold of salt concentration, the gain obtained by reducing the ohmic drop inside a MES is lost by the inhibition of the microbial catalysis on the electrode(s). This is the reason why most MESs have been implemented in electrolytes with conductivities of the order of 1 S m^{-1} . For example, Lefebvre *et al.* have shown that the power produced by a microbial fuel cell increases for NaCl concentrations up to 20 g L^{-1} and then decreases by 50% for 40 g L^{-1} .⁴⁰ Many attempts have been made to increase the ionic conductivity of the solutions in which bioanodes can be effective. Microbial fuel cells have been designed in seawater, directly in seas and oceans,⁴¹ or marine inocula have been implemented under laboratory conditions.^{42–44} Pure strains have also shown some halotolerance.^{45–47} *Geobacter sulfurreducens* (KN400) has been adapted to marine salinity with some success.⁴⁸ Recently, the halophilic strain *Geoalkalibacter subterraneus* has provided 3.3 A m^{-2} under polarization at $-0.2 \text{ V vs. Ag/AgCl}$ in a solution containing 17 g L^{-1} NaCl (half seawater salinity)⁴⁹ and up to 4.7 A m^{-2} at $+0.2 \text{ V/SCE}$ in another study with 35 g L^{-1} NaCl.⁵⁰ A wild inoculum coming from a salt marsh has boosted the current density provided by bioanodes to 70 A m^{-2} in an electrolyte containing 45 g L^{-1} NaCl (conductivity 10.4 S m^{-1}) but the current was smaller at 60 g L^{-1} NaCl (conductivity 13.5 S m^{-1}).⁵¹

In the current state of the art, the upper limit of the ionic conductivities at which microbial anodes can be implemented is around the level of seawater conductivity, with only one example reaching conductivities above 10 S m^{-1} .⁵¹ The model described here showed that even seawater conductivity (5.3 S m^{-1}) was not sufficient to avoid a drastic current gradient along a bioanode that exhibited efficient electrocatalytic properties. For comparison, it

can be recalled that industrial electrolysis processes function with electrolytes of considerably higher ionic conductivity. For example, the production of hydrogen by conventional water electrolysis, implemented in 33% by mass KOH, benefits from a conductivity of 60 S m^{-1} . The crucial impact of electrolyte conductivity on reactor design, which has been evidenced here, is intrinsically linked to the microbial aspect of MESSs. Modelling will consequently be an indispensable tool in the scaling up of MESSs.

Considering the anode kinetics used as the standard in the present work ($j_{\text{max}} = 5.8 \text{ A m}^{-2}$) and the common conductivity value of 1 S m^{-1} , the total currents that flowed through the whole MEC were 23.6 mA and 25.6 mA for the parallel and perpendicular configurations respectively. The perpendicular configuration thus offered only a very slight advantage (8% improvement) with respect to the parallel configuration, and probably at the cost of greater technological complexity. In any case, the doubling of currents that could be expected because the perpendicular configuration allows a double anode surface area to be exposed to the solution in comparison to the parallel configuration was far from being reached. Actually, the ohmic drop increase along the anode abolished the advantage that the design was hoped to offer in terms of the anode surface area. Plotting the impact of the electrolyte conductivity from 0.5 to 6 S m^{-1} (Fig. 5A) fully confirmed the above conclusion. It even showed that, at the lowest conductivities, the perpendicular configuration provided less current than the parallel one.

Optimising the cathode–anode distance. At low conductivity (1.0 S m^{-1}) the distance between the anode and cathode had a major effect on the global current for both the parallel and perpendicular configurations (Fig. 5B). In both configurations, around 40% of current was lost when the distance increased from 1 to 10 cm. At high conductivity (5.3 S m^{-1}) the perpendicular geometry showed its better capacity by producing up to 30% more current than the parallel configuration. Nevertheless, the performance of the perpendicular configuration remained far below twice that of the parallel one, as could be expected. At the highest conductivity, the two configurations showed a constant difference, whatever the distance between the electrodes (Fig. 5B). In this case, the perpendicular geometry, even with the anode and cathode 10 cm apart gave higher current than the parallel configuration with a separation of only 5 mm. The high conductivity of the electrolyte was confirmed to be the key parameter that determined whether or not full advantage could be taken of the design.

As a general rule, it can be concluded that, at the lowest conductivities (here $< 1 \text{ S m}^{-1}$), the parallel configuration gives higher total current. Both configurations produce currents of the same level and, for the sake of simplicity, the parallel configuration remains the most suitable at low conductivities (here $< 2 \text{ S m}^{-1}$), while the perpendicular configuration starts to be justified at higher conductivities. The values around 1 and 2 S m^{-1} obtained here for the two thresholds are not absolute values and will vary according to the characteristics of the bioanode kinetics.

Influence of cell voltage. Fig. 6 compares current densities for cell voltages ranging from 0.6 to 1.0 V. The increase of the cell voltage obviously has a great impact on current density.

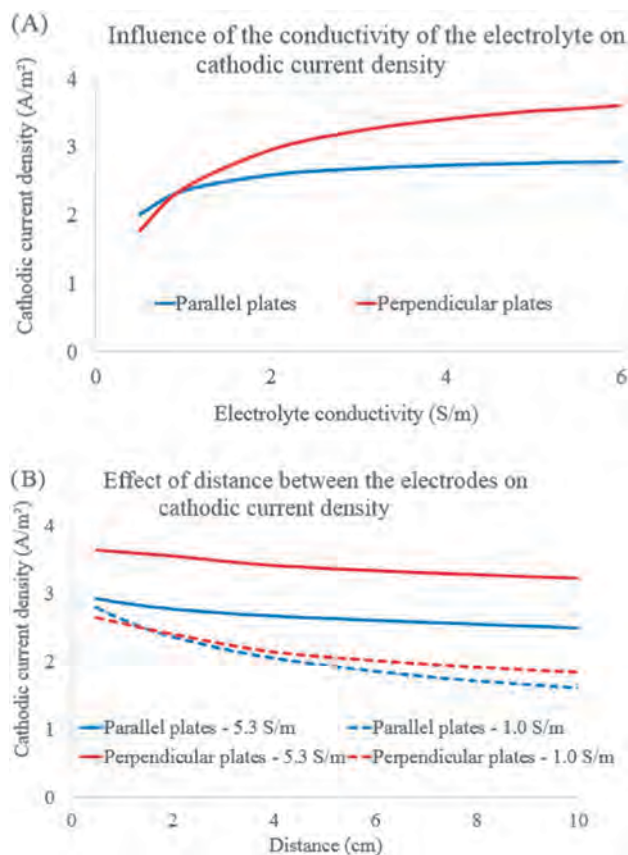


Fig. 5 Influence on the average cathodic current density of (A) electrolyte conductivity (distance between anode and cathode 2 cm) and (B) distance between anode and cathode (conductivity 1.0 or 5.3 S m^{-1}); in each case the cell voltage was 0.8 V.

On average, an increase of 0.2 V multiplied the current by a factor between 2 and 3. Once again, the low conductivity brought the performance of the perpendicular configuration down to the same order of magnitude as the parallel configuration. The calculations also showed that the perpendicular configuration became more and more suitable as the cell

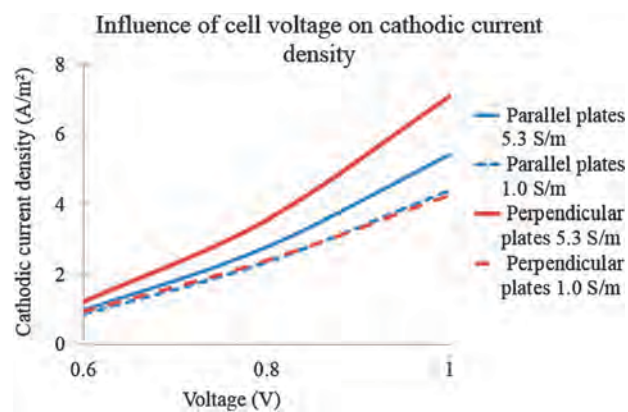


Fig. 6 Average cathodic density as a function of the cell voltage for the conductivities 1.0 and 5.3 S m^{-1} , anode–cathode distance 2 cm, perpendicular and parallel configurations.

voltage increased. These data can be used to estimate the cost of hydrogen production and to compare it with conventional water electrolysis in alkaline cells. Considering an MEC designed with perpendicular electrodes 2 cm apart and an electrolyte with a conductivity of 5.3 S m^{-1} , the amount of energy spent to produce 1 m^3 of hydrogen (standard conditions) under 0.8 V is 1.8 kW h, compared to 4.4–5.4 kW h for commercial alkaline electrolyzers.⁵²

3.4 Optimizing the anode surface area

Increasing the total surface area of the anode is an obvious way to counterbalance the current limitation due to bioanode kinetics. The perpendicular configuration allowed the number of anode plates to be multiplied easily. The model was run with the high value of conductivity only (5.3 S m^{-1}), which allowed better implementation of the perpendicular configuration. The cell voltage and the cathode–anode distance were kept constant at 0.8 V and 2 cm respectively.

Six geometries having one to six identical anodes were modelled. The electrodes were arranged to have equal distances between them (Fig. 7A). It might be thought that using a stack of horizontal anodes would raise technical problems for CO_2 evacuation. It should be noted that the rate of CO_2 evolution at the anode is half the rate of H_2 evolution at the cathode (reactions (14) and (15)). Moreover, the total anode surface area being two to six times greater than the cathode surface area, the density of CO_2 production is diminished in the same proportion. Under such conditions of low local CO_2 evolution, gas evacuation can be ensured by a slow flow or gentle stirring of the electrolyte. If necessary, the anodes could be slightly tilted with respect to the horizontal and/or made up of grids. These architectures could be fed into the model, but this would lead to complex technical discussions, which are not the objective of the present study.

The total current that flowed through the cell was proportional to the current density of cathode since the cathode had always the same surface area in any architecture. The total current obtained with 6 anodes was 62 mA (6.2 A m^{-2} average current density on the cathode) compared to 36 mA when only one anode was used (Fig. 7B). The multiplication of the anode plates was far from multiplying the whole current by the same factor. The average current densities on each anode face showed that each side of the anode(s) produced less and less current as their number increased. Actually, each anode worked under worse conditions when the anode stack became denser. Degradation of the anode working conditions was obvious when the potential distribution for the different geometries was plotted. A glance at the colour chart (Fig. 8) shows that the electrostatic potential inside the anode stack (ϕ_{SA}) increased significantly with the number of plates. As the Nernst potential of the anode (E_A) varies inversely to the electrostatic potential of the solution (eqn (22)) the bioanodes worked at decreasing Nernst potential as the stack became denser.

The values of the electrostatic potential of the electrolyte against the anode surface (ϕ_{SA}) at the points farthest from the cathode (points 1 to 3 in Fig. 8) were 1.101, 1.172 and 1.217 V respectively, which corresponded to local Nernst potentials of -0.301 , -0.372

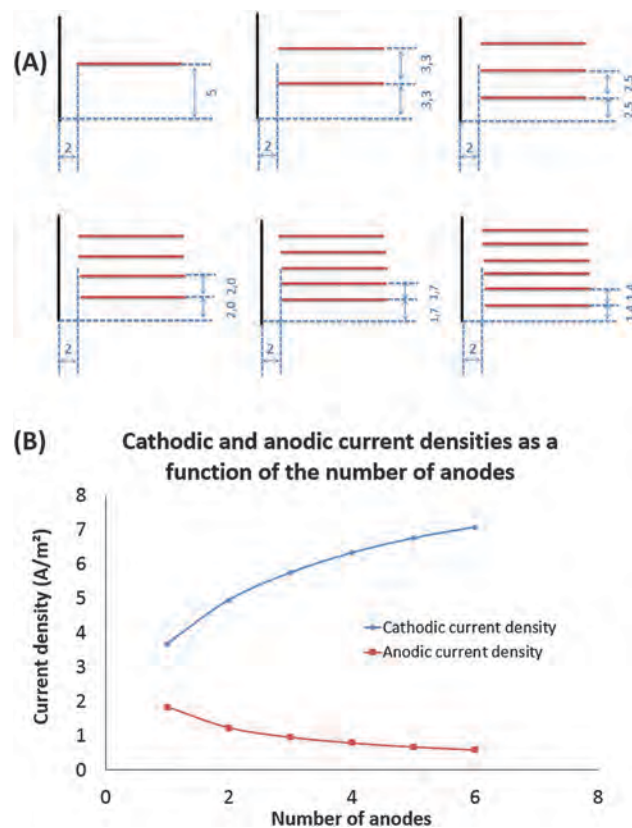


Fig. 7 Stack of perpendicular bioanodes. (A) Position of the electrodes in the stacks of 1 to 6 anodes (distances are expressed in centimetres). (B) Influence of the number of anode plates on average anodic and cathodic current densities. The average current densities were calculated with respect to each electrode side (for instance, the anode surface area was 2 times that of the cathode in the one-plate geometry and 12 times in the 6-plate geometry). Conductivity 5.3 S m^{-1} ; cell voltage 0.8 V.

and -0.417 V/SCE . The deep parts of the bioanodes were considerably impeded by the densification of the stack. The same conclusion was obvious when the local current densities at the same deep internal positions, which were 1.74, 0.87 and 0.42 A m^{-2} respectively, were considered. When the distance between the plates is too low, the ionic flow is impeded, resulting in higher electrostatic potential in the deep internal parts of the anode stack.

As a general rule, it can be concluded that the internal design of a bioanode stack, or more generally of a three-dimensional bioanode, must be carefully considered. A simple increase of the active surface area in a given volume is not sufficient, because densifying the internal electrode network results in worsening of the internal electrochemical conditions. This general conclusion can explain previous experimental observations made with porous three-dimensional electrodes. The most appropriate carbon foams to support microbial bioanodes reported in the literature combine high porosity (98%) and large pore size ($300\text{--}500 \mu\text{m}$).^{29,53} It has been explained that high porosity logically maximises the penetration of microorganisms and the diffusional substrate supply, and the large pore size avoids pore clogging by the biofilm.⁵⁴ The model developed here gives a supplementary explanation. It demonstrates that a large pore size is also necessary to avoid a

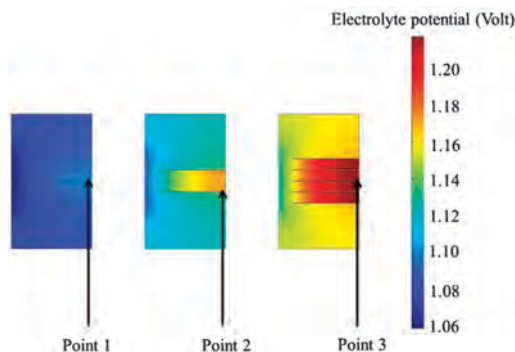


Fig. 8 Distribution of the electrostatic potential in solution (ϕ_s) in an MEC with perpendicular electrodes. The bioanode (horizontal) was composed of a stack of one, two or five electrodes (geometry detailed in Fig. 7A). Conductivity 5.3 S m^{-1} ; cell voltage 0.8 V . The red colour indicates a higher ϕ_s , i.e. a lower Nernst potential of the anode (E_A). The multiplication of the anodes increased the electrostatic potential at their surface leading to degraded conditions inside the multi-anode system.

drastic increase of the electrostatic potential of the electrolyte inside the structure.

4. Experimental

4.1 Model validation with the conventional abiotic electrolysis of water

Water electrolysis was carried out in a lab-scale electrolyser, which consisted of two 13 cm^2 ($6.5 \times 2 \text{ cm}$) parallel electrodes made of 316 L stainless steel and 6 cm apart. The electrolyte was distilled water with three different concentrations of sodium sulphate that gave ionic conductivities of 0.85 , 2.41 and 4.25 S m^{-1} . The cell voltage was measured for the different currents that were applied to the cell (intentional mode, Biologic potentiostat). For each current value, the voltage stabilized in less than 10 min .

The current–potential (j – E) curves required as input for the model were determined separately for the anode and the cathode. A saturated calomel reference electrode (SCE, 0.241 V vs. SHE) was set as close as possible to the electrode under study and in the electrolyte with the highest conductivity (4.25 S m^{-1}) to avoid bias due to the ohmic drop between the tip of the reference electrode and the working electrode surface.

4.2 Anode and cathode kinetics of the MEC (boundary conditions)

The cathode boundary condition was determined experimentally using a 15 cm^2 stainless steel cathode in a solution that contained 10 mM phosphate buffer. The experimental j – E curve was fitted with the polynomial function (Fig. 9):

$$j = -1941.9E^4 - 7742.7E^3 - 11634E^2 - 7784.7E - 1953.8 \quad (R^2 = 0.9993) \quad (24)$$

where j is the current density (A m^{-2}) and E is the potential vs. the calomel reference electrode (V/SCE), which was used as the cathode boundary condition in the model. A Butler–Volmer

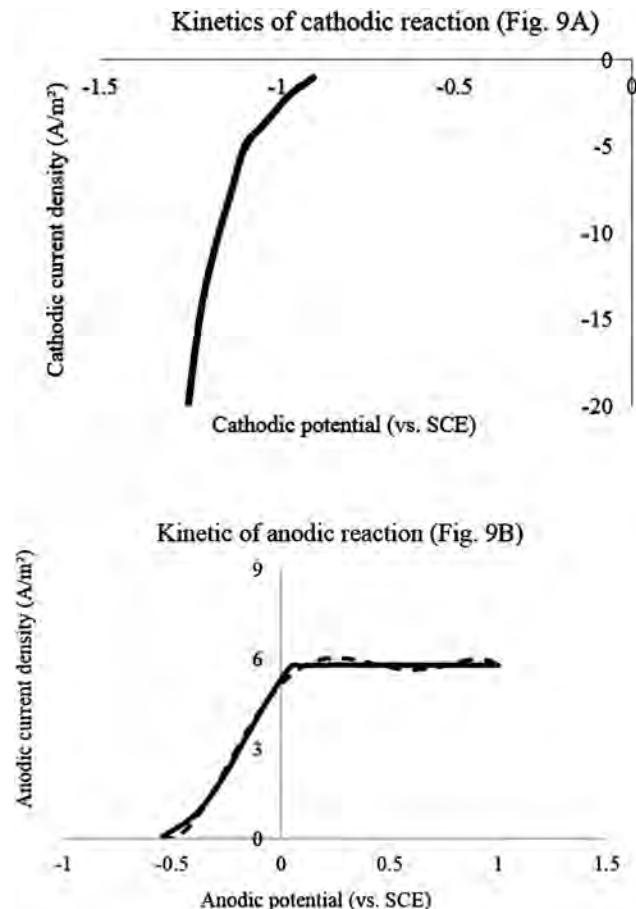


Fig. 9 Fitting of experimental cathode (A) and anode (B) boundary conditions. Solid line: experimental data; dotted line: polynomial fitting.

equation might also be used to fit this abiotic kinetics but, in this case, it was numerically less accurate than the polynomial approach used here.

The “standard” anode boundary condition corresponded to a microbial anode formed on carbon cloth in seawater inoculated with marine sediments. It gave a maximum current density of 5.8 A m^{-2} at $+0.1 \text{ V/SCE}$. The experimental j – E curve reported in the literature³⁹ was fitted with the polynomial function:

$$j = -3.7484E^6 - 15.46E^5 + 32.968E^4 - 3.5113E^3 - 17.177E^2 + 7.5458E + 5.1706 \quad (R^2 = 0.9958) \quad (25)$$

which was used to feed the model. Obviously, this equation had no physical meaning it was used only as an appropriate numerical approach. Actually, the experimental j – E curve was available only for potentials ranging from -0.5 to $+0.1 \text{ V/SCE}$ and this range was sufficient to model the MEC. Nevertheless, the model may need values of potential above the 0.1 V limit for intermediate iterative calculations. It was consequently necessary to limit the current densities by extending the polynomial function beyond 0.1 V/SCE with a constant plateau at 5.8 A m^{-2} (Fig. 9). The final potential distribution did not use potentials above $+0.1 \text{ V}$ but this precaution avoided possible divergence during numerical solving.

A more efficient kinetics was also used in some cases for comparison at low electrolyte conductivity. This anode extracted from the literature was formed on carbon cloth in garden compost leachate.³⁰ It allowed current densities around 34 A m^{-2} be reached from potentials as low as -0.3 V/SCE . In this case, it was possible to accurately fit the experimental data with a Nernst–Monod equation (eqn (20)).³⁰

4.3 Numerical modelling

Two MEC geometries were considered for modelling: parallel, face to face cathode and anode on the one hand, and horizontal anode(s) perpendicular to a vertical cathode on the other. In each case, the electrodes were $(10 \times 10) \text{ cm}^2$ square and located at a central, non-conducting wall of 20 cm length. The set of regular parameters was: abiotic cathode boundary condition, “standard” bioanode boundary condition ($j_{\max} = 5.8 \text{ A m}^{-2}$), electrolyte ionic conductivity 1 S m^{-1} , distance between cathode and anode 2 cm , cell voltage 0.8 V .

The model was developed using Comsol Multiphysics (r) v3.5 with the conductive media DC module. The integration space was discretized with free mesh parameters (triangles) having an extra-fine predefined mesh size. A maximum of 4142 elements were used for the perpendicular MEC configuration. Average current densities over each electrode were calculated with the post-processing integration module. The internal electrostatic potential against the bioanode surface (ϕ_{SA} , Fig. 8) was extracted using the post-processing Comsol function.

5. Conclusion

The experimental attempts made so far to scale up MESSs have highlighted the great difficulty of the challenge in the absence of theoretical support for reactor design. The first foray into modelling potential distribution in MES, described here, should be of great help in the scaling-up work by providing a solid and fairly easy-to-handle theoretical support. Modelling the secondary distribution of the potential should now be considered as an essential basic tool in developing large-scale MESSs. More sophisticated approaches could be contemplated in the future, including tertiary distribution, impact of gas bubbling on the electrolyte conductivity, and electronic heterogeneities inside three-dimensional macro-porous electrodes but, in its present state, the theoretical basis detailed here are sufficient to extract sound, simple scaling-up rules.

General rules can be stated. For example, a perpendicular configuration is justified only if the conductivity of the solution is high enough to take advantage of it. Increasing the active surface area in a given volume should not be the only objective and care must be simultaneously taken to minimize the increase of internal electrostatic potential that is induced by the densification of the bioanode. These rules are considerably more important for MESSs than for conventional electrochemical systems, because of the low ionic conductivities at which MESSs are most often constrained to operate. Using a theoretical approach appears to be essential to identify the narrow and difficult pathway that could lead to optimal large-scale MESSs.

Abbreviations

$C_{\text{acetate}}^{\text{B}}$	Concentration of acetate in the solution bulk (mol m^{-3})
$C_{\text{acetate}}^{\text{int}}$	Concentration of acetate at the biofilm/solution interface (mol m^{-3})
D_{acetate}	Diffusion coefficient of acetate ($1.2 \times 10^{-9} \text{ m}^2 \text{ s}^{-1}$) ⁵⁵
E	Nernst potential (V)
E_{A}	Nernst potential at the anode (V)
E_{C}	Nernst potential at the cathode (V)
$E^{0'}$	Formal potential of a redox couple (V)
$E_{1/2}$	Potential at $j = j_{\max}/2$ in the Nernst–Monod equation (V)
f_{A}	Relation between potential and current density used as boundary condition at the anode (biofilm-driven electrochemical kinetics)
f_{C}	Relation between potential and current density used as boundary condition at the cathode (kinetics for hydrogen evolution)
F	Faraday constant ($96485 \text{ Coulomb mol}^{-1} \text{ e}^{-1}$)
i	Electrical current (A)
j	Electrical current density (A m^{-2})
j_{\max}	Maximum current density in the Nernst–Monod equation (A m^{-2})
\vec{n}	Vector normal to a surface
U_{cell}	Cell voltage (V)
δ	Diffusion layer thickness (m)
ϕ	Electrostatic potential (V)
ϕ_{MA}	Electrostatic potential in the anode material (V)
ϕ_{MC}	Electrostatic potential in the cathode material (V)
ϕ_{S}	Electrostatic potential in solution (V)
ϕ_{SA}	Electrostatic potential in solution at the biofilm/solution interface (V)
ϕ_{SC}	Electrostatic potential in solution at the cathode surface (V)
Φ_{acetate}	Molar flux of acetate ($\text{mole m}^{-2} \text{ s}^{-1}$)
σ	Electrolyte ionic conductivity (S m^{-1})
$ _{\text{SA}}$	Derivation at the biofilm/solution interface (anode)
$ _{\text{SC}}$	Derivation at the cathode surface

Acknowledgements

This research was part of the “DefiH12” project funded by the French National Research Agency (ANR-09-BioE-010).

Notes and references

- 1 B. E. Logan and K. Rabaey, *Science*, 2012, **337**, 686–690.
- 2 Article pionier MEC sans doute: H. Liu, S. Grot and B. E. Logan, *Environ. Sci. Technol.*, 2005, **39**, 4317–4320.
- 3 R. A. Rozendal, H. V. M. Hamelers, G. J. W. Euverink, S. J. Metz and C. J. N. Buisman, *Int. J. Hydrogen Energy*, 2006, **31**, 1632–1640.

- 4 S. Cheng and B. E. Logan, *Bioresour. Technol.*, 2011, **102**, 4468–4473.
- 5 B. E. Logan, *Appl. Microbiol. Biotechnol.*, 2010, **85**, 1665–1671.
- 6 I. Ieropoulos, J. Greenman and C. Melhuish, *Int. J. Energy Res.*, 2008, **32**, 1228–1240.
- 7 A. Dewan, H. Beyenal and Z. Lewandowski, *Environ. Sci. Technol.*, 2008, **42**, 7643–7648.
- 8 V. B. Oliveirab, M. Simõesb, L. F. Melob and A. M. F. R. Pintoa, *Biochem. Eng. J.*, 2013, **73**, 53–64.
- 9 L. Hsu, B. Chadwick, J. Kagan, R. Thacher, A. Wotawa-Bergen and K. Richter, *RSC Adv.*, 2013, **36**, 15947–15954.
- 10 C. I. Torres, A. K. Marcus, H.-S. Lee, P. Parameswaran, R. Krajmalnik-Brown and B. E. Rittmann, *FEMS Microbiol. Rev.*, 2010, **34**, 3–17.
- 11 C. Picioreanu, I. M. Head, K. P. Katuri, M. C. M. van Loosdrecht and K. Scott, *Water Res.*, 2007, **41**, 2921–2940.
- 12 A. K. Marcus, C. I. Torres and B. E. Rittmann, *Biotechnol. Bioeng.*, 2007, **98**, 1171–1182.
- 13 B. V. Merkey and D. L. Chopp, *Bull. Math. Biol.*, 2012, **74**, 834–857.
- 14 H. Richter, K. P. Nevin, H. F. Jia, D. A. Lowy, D. R. Lovley and L. M. Tender, *Energy Environ. Sci.*, 2009, **2**, 506–516.
- 15 S. M. Strycharz, A. P. Malanoski, R. M. Snider, H. Yi, D. R. Lovley and L. M. Tender, *Energy Environ. Sci.*, 2011, **4**, 896–913.
- 16 C. I. Torres, A. K. Marcus and B. E. Rittmann, *Biotechnol. Bioeng.*, 2008, **100**, 872–881.
- 17 P. S. Bonanni, G. D. Schrott, L. Robuschi and J. P. Busalmen, *Energy Environ. Sci.*, 2012, **5**, 6188–6195.
- 18 H. V. M. Hamelers, A. Ter Heijne, N. Stein, R. A. Rozendal and C. J. N. Buisman, *Bioresour. Technol.*, 2011, **102**, 381–387.
- 19 H.-S. Lee, C. I. Torres and B. E. Rittmann, *Environ. Sci. Technol.*, 2009, **43**, 7571–7577.
- 20 D. Pocaznoi, B. Erable, L. Etcheverry, M.-L. Délia and A. Bergel, *Phys. Chem. Chem. Phys.*, 2012, **14**, 13332–13343.
- 21 B. Cercado, N. Byrne, M. Bertrand, D. Pocaznoi, M. Rimboud, W. Achouak and A. Bergel, *Bioresour. Technol.*, 2013, **134**, 276–284.
- 22 B. E. Logan, B. Hamelers, R. Rozendal, U. Schröder, J. Keller, S. Freguia, P. Aelterman, W. Verstraete and K. Rabaey, *Environ. Sci. Technol.*, 2006, **40**, 5181–5192.
- 23 L. De Silva Munoz, A. Bergel, D. Féron and R. Basseguy, *Int. J. Hydrogen Energy*, 2010, **35**, 8561.
- 24 L. De Silva Munoz, B. Erable, L. Etcheverry, J. Riess, R. Basseguy and A. Bergel, *Electrochem. Commun.*, 2010, **12**, 183–186.
- 25 S. C. Dexter and S. H. Lin, *Corrosion*, 1992, **48**, 50–60.
- 26 A. G. Zelinsky and B. Ya. Pirogov, *Russ. J. Electrochem.*, 2008, **44**, 585–593.
- 27 V. S. Bagotsky, *Fundamentals of electrochemistry*, John Wiley & Sons Inc., Hoboken (New Jersey), 2nd edn, 2006, p. 66.
- 28 Y. Liu, F. Harnish, U. Schröder, K. Fricke, V. Climent and J. M. Feliu, *Biosens. Bioelectron.*, 2010, **25**, 2167–2171.
- 29 S. Chen, H. Hou, F. Harnish, A. S. Patil, A. Carmona-Martinez, S. Argawal, Y. Zhang, S. Sinya-Ray, L. A. Yarin, A. Greiner and U. Schröder, *Energy Environ. Sci.*, 2011, **4**, 1417–1421.
- 30 D. Pocaznoi, A. Calmet, L. Etcheverry, B. Erable and A. Bergel, *Energy Environ. Sci.*, 2012, **5**, 9645–9652.
- 31 D. Pocaznoi, B. Erable, M.-L. Délia and A. Bergel, *Energy Environ. Sci.*, 2012, **5**, 5287–5296.
- 32 S. Chen, G. He, Q. Liu, F. Harnish, Y. Zhou, Y. Chen, M. Hanif, S. Wang, X. Peng, H. Hou and U. Schröder, *Energy Environ. Sci.*, 2012, **5**, 9769–9772.
- 33 R. A. Rozendal, A. W. Jeremiasse, H. V. M. Hamelers and C. J. N. Buisman, *Environ. Sci. Technol.*, 2008, **42**, 629.
- 34 M. D. Merrill and B. E. Logan, *J. Power Sources*, 2009, **191**, 203.
- 35 B. Tartakovsky, M.-F. Manuel, H. Wang and S. R. Guiot, *Int. J. Hydrogen Energy*, 2009, **34**, 672.
- 36 A. W. Jeremiasse, H. V. M. Hamelers and C. J. N. Buisman, *Bioelectrochemistry*, 2010, **78**, 39.
- 37 R. A. Cox, F. Culkin and J. P. Riley, *Deep-Sea Res. Oceanogr. Abstr.*, 1967, **14**, 203.
- 38 S. DaSilva, R. Basseguy and A. Bergel, *Electrochim. Acta*, 2004, **49**, 4553–4561.
- 39 B. Erable and A. Bergel, *Bioelectrochemistry*, 2009, **100**, 3302–3307.
- 40 O. Lefebvre, Z. Tan, S. Kharkwal and H. Y. Ng, *Bioresour. Technol.*, 2012, **112**, 336–340.
- 41 M. E. Nielsen, C. E. Reimers, H. K. White, S. Sharma and P. R. Girguis, *Environ. Sci. Technol.*, 2012, **106**, 89–94.
- 42 B. Erable, M. A. Roncato, W. Achouak and A. Bergel, *Environ. Sci. Technol.*, 2009, **43**, 3149–3199.
- 43 C. Dumas, A. Mollica, D. Féron, R. Basseguy, L. Etcheverry and A. Bergel, *Bioresour. Technol.*, 2008, **99**, 8887–8894.
- 44 S. J. You, J. N. Zhang, Y. X. Yuan, N. Q. Ren and X. H. Wang, *J. Chem. Technol. Biotechnol.*, 2010, **85**, 1077–1083.
- 45 J. H. Yoon, S. H. Yeo, T. K. Oh and Y. H. Park, *Int. J. Syst. Evol. Microbiol.*, 2004, **54**, 1197–1201.
- 46 Y. Wang, H. Wang, J. W. Liu, Q. L. Lai, Z. Z. Shao, B. Austin and X. H. Zhang, *FEMS Microbiol. Lett.*, 2010, **309**, 48–54.
- 47 I. Vandecandelaere, O. Necessian, E. Segart, W. Achouak, A. Mollica, M. Faimali, P. De Vos and P. Vandamme, *Int. J. Syst. Evol. Microbiol.*, 2008, **58**, 2589–2596.
- 48 K. P. Nevin, P. Zhang, A. E. Franks, T. L. Woodard and D. R. Lovley, *J. Power Sources*, 2011, **196**, 7514–7518.
- 49 J. P. Badalmenti, R. Krajmalnik-Brown and C. I. Torres, *mBio*, 2013, **4**, 1–8.
- 50 A. A. Carmona-Martinez, M. Pierra, E. Trably and N. Bernet, *Phys. Chem. Chem. Phys.*, 2013, **15**, 19699–19707.
- 51 R. Rousseau, X. Dominguez-Benetton, M.-L. Délia and A. Bergel, *Electrochem. Commun.*, 2013, **33**, 1–4.
- 52 J. A. Turner, *Science*, 2004, **305**, 972–974.
- 53 S. Chen, Q. Liu, G. He, Y. Zhou, M. Hanif, X. Peng, S. Wang and H. Hou, *J. Mater. Chem.*, 2012, **22**, 18609–18613.
- 54 S. F. Ketep, A. Bergel, A. Calmet and B. Erable, *Energy Environ. Sci.*, 2014, **7**, 1633–1637.
- 55 D. G. Leaist and P. A. Lyons, *J. Solution Chem.*, 1984, **13**, 77–85.